JGR Atmospheres

RESEARCH ARTICLE

Key Points:

- Indian Ocean Basin mode (IOBM) in preceding Jan-Mar plays a crucial role on the Apr-Jun precipitation in western Northwest China (WNWC)
- The close lagged relationship between IOBM and WNWC precipitation is unstable, and varies with Pacific Decadal Oscillation (PDO)
- The IOBM-based statistical rainfall prediction scheme on WNWC has a high predictability during the cold phase of PDO

Correspondence to:

J. Huang,
hjp@lzu.edu.cn

Enhanced Impacts of Indian Ocean Sea Surface Temperature on the Dry/Wet Variations Over Northwest China

Shanshan Wang[1], Jianping Huang[1] , Gang Huang[2] , Fu Luo[1], Yulong Ren[3], and Yongli He[1]

[1]Key Laboratory for Semi-Arid Climate Change of the Ministry of Education, College of Atmospheric Sciences, Lanzhou University, Lanzhou, China, [2]State Key Laboratory of Numerical Modeling for Atmospheric Sciences and Geophysical Fluid Dynamics (LASG), Institute of Atmospheric Physics, Chinese Academy of Sciences, Beijing, China, [3]Key Laboratory of Arid Climatic Change and Reducing Disaster of Gansu Province, and Key Open Laboratory of Arid Climate Change and Disaster Reduction of CMA, Institute of Arid Meteorology, CMA, Lanzhou, China

Abstract Most western Northwest China (WNWC) has experienced notable wetting in recent decades. Despite the widespread attention of scientific community, the causes of such climate shift are still not well-understood. In this study, we find that the dominant mode of Indian Ocean sea surface temperature variability — Indian Ocean Basin mode (IOBM) plays a crucial role in the precipitation over WNWC. Nonetheless, such a close lagged relationship is unstable, and varies with Pacific Decadal Oscillation (PDO). When the PDO is in its warm phase, there is no robust lagged relationship between April-June WNWC precipitation variations and January-March IOBM. When the PDO is in its cold phase, the warm phase of the IOBM inspires a wavetrain across the Eurasian continent in the next April-June, with an uncommon low pressure around Lake Baikal, thereby enhancing the westerlies and thus more moisture into the WNWC region. This enables the IOBM-based statistical rainfall prediction scheme to estimate the precipitation in the WNWC region with some confidence. This remarkable contrast in the influence of IOBM between the two phases of the PDO highlights exciting new avenues for improving climate predictions over the WNWC.

Plain Language Summary The preceeding January-March Indian Ocean Basin mode (IOBM) plays a crucial role on early summer precipitation in WNWC. But such high lagged-relationship is not stable and varies with the Pacific Decadal Oscillation (PDO). When the PDO is in warm phase, there is no robust lagged-relationship between April-June WNWC precipitation variations and January-March IOBM. While the PDO is in cold phase, the warm IOBM inspires a wavetrain across Eurasian in next April-June, with an anomalous low pressure around Lake Baikal, thereby enhancing the westerlies and thus more moisture into WNWC region. So is the success of an IOBM-based statistical rainfall prediction scheme on WNWC.

1. Introduction

The arid and semi-arid regions of western Northwest China (WNWC) are located at the Eurasian continent's hinterland and lie in the shadow of the Tibetan Plateau (Figure 1; Peng & Zhou, 2017; Shen et al., 2020; Yao et al., 2020). Unlike eastern monsoonal China, the climate in WNWC is mainly influenced by the subtropical westerly circulation (Chen, Zhang, et al., 2021; Shen et al., 2020). The annual precipitation is typically below 200 mm and the ecologic environment is relatively fragile (Huang et al., 2008, 2017; Koster et al., 2004). However, WNWC is one of China's key agricultural production bases due to its long sunshine duration and large diurnal temperature range. Even small precipitation changes would significantly affect the local agriculture production and economy in this region, especially during the key stage of crop emergence and growth in spring and summer. For example, a torrential rainfall event hit the Korla area on 4 June 2012, causing floods, landslides and debris flows, thereby leading to severe lives and property damage (Chen et al., 2015). During April-August 2014, a prolonged drought in Xinjiang province affected over 287,000 ha of crops and 1.5 million hectares of pastures, causing a direct economic loss exceeding 4.3 billion RMB (about $700 million, http://www.chinadaily.com.cn/china/2014-08/23/content_18475075.htm).

In general, the precipitation of WNWC is mainly contributed by the water vapor transported from the North Atlantic, Black Sea and the Caspian Sea and evapotranspiration in Eurasia (termed as the western channel), and the water vapor from the Arctic Ocean (termed as the northern channel) (Dai et al., 2007; Drumond et al., 2011). These two water vapor channels are highly influenced by the Arctic Oscillation (AO) and North
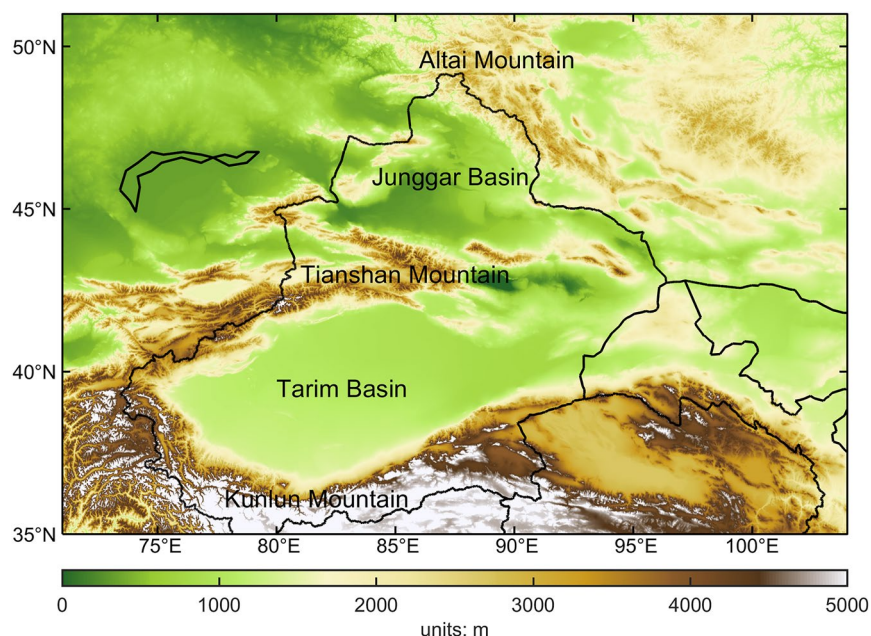
Figure 1. Map of the study region. Color shading indicates the topographic height.

Atlantic Oscillation (NAO), and meanwhile the El Niño-Southern Oscillation (ENSO) also plays a crucial role on the western channel into the WNWC via atmospheric teleconnection (Li et al., 2005; Shen et al., 2020; Yao et al., 2020). In addition, a recent study suggested that another water vapor channel from the Indo-Pacific Ocean has caused a higher precipitation in WNWC due to the weakened East Asian summer monsoon with westward and northward western Pacific subtropical High (WPSH) (Chen, Zhang, et al., 2021).

Additionally, the tropical Indian Ocean (TIO) sea surface temperature (SST) anomaly is perceived to play an essential role in the Asian monsoon (Kucharski et al., 2006; Xie et al., 2002; Yang et al., 2007). As the dominant mode of SST variability in the TIO basin, the Indian Ocean basin mode (IOBM) exhibits basin-wide warming that peaks in late winter and persists into the following spring and summer after an El Niño event (Yang et al., 2007). The IOBM can induce robust climatic anomalies in the Indo-West Pacific region, prolonging the El Niño's influence after the tropical East Pacific SST returns to normal (Xie et al., 2002). Nevertheless, the IOBM is not just a passive response to El Niño but an important driver of summer climate variability in the East Asia region, via forcing a Matsuno-Gill pattern in the upper troposphere with a strengthened South Asian High (SAH) (Schott et al., 2009; Yang et al., 2007). Previous studies reported that the associated wave-like circulation with summer precipitation in WNWC is the extratropical response to the tropical heating from the Indian Ocean (e.g., Chen & Huang, 2012; Li & Ma, 2018). Huang et al. (2015) observed that the Indian summer monsoon (ISM) associated circulation pattern could bring low-level water vapor from the Indian Ocean to WNWC along the eastern periphery of the Tibetan Plateau (Huang et al., 2015). Recently, by analyzing the relationship between the IOBM and precipitation in the eastern part of Northwest China (ENWC), Yang et al. (2015) found that the persisting anomaly of the IOBM in the previous winter and spring is significantly correlated with the subsequent May precipitation change in ENWC. However, it is known that climate responses are distinctly different in spatial distribution over the arid and semi-arid regions of Northwest China (i.e., drying in the east and wetting in the west) in recent decades (Wang et al., 2020; Zhang, Lin, et al., 2019; Zhang, Yang, et al., 2019). Therefore, this study shall extend these studies by investigating to what extent and how the IOBM affects the dry-wet variations in WNWC.

Moreover, the arid and semi-arid regions of WNWC are susceptible to global climate change (Shen et al., 2020; Shi et al., 2007). Recently, many studies have indicated the detectable warming and wetting trends in the WNWC region (e.g., Li et al., 2010; Peng & Zhou, 2017; Shi et al., 2007). Over the past several decades, hydrological extremes (e.g., drought and flood) have strengthened (in terms of frequency and intensity) in many parts of WNWC (Shen et al., 2020; Wang et al., 2015; Zhang, Chen, & Zhang, 2019). Meanwhile, existing records

of IOBM SST exhibit clear fluctuations include a rising trend since the 1960s and decadal variability (Han et al., 2014; Qu & Huang, 2012). In comparison with decadal climate variability in the Atlantic and Pacific Oceans that have been extensively studied, the decadal variability of the Indian Ocean is much less understood. Recently, some research suggests that part of it may be caused by natural decadal variability in Pacific — the decadal oscillation (PDO) (Han et al., 2014). In general, the PDO affects the Indian Ocean via atmospheric and oceanic teleconnections (Cole et al., 2000; Huang et al., 2019). Statistically, the PDO index is positively correlated with the IOBM index (Hong et al., 2021). However, recent studies suggested that the relationship of decadal PDO and IOBM is not stationary and became negative in the past decades (Dong & McPhaden, 2017; Han et al., 2014; Hong et al., 2021). In the context of climate change mentioned above, a good understanding of the relationship between IOBM and dry/wet conditions of the WNWC, and the significance of IOBM on wetting over the WNWC are necessary. Such knowledge is of great scientific and societal importance to the ecological environment and social development.

2. Data and Methods

2.1. Data

Daily rainfall data (1961–2018; 839 stations) are downloaded from the National Meteorological Information Center (NMIC), China Meteorological Administration (CMA), which has resolved the problems of incorrect and missing data caused by digitization and restoring of historical basic meteorological data (Ren et al., 2012) and converted to monthly means. Based on the CMA/NMIC data, precipitation index (PI) is defined as standardized precipitation anomaly averaged over the area 35°-50°N, 70°-100°E to represent the intensity of the dry-wet variability across the WNWC. We obtain SST data set from the monthly Extended Reconstructed Sea Surface Temperature, version 5 (ERSST.v5; Huang et al., 2017). Monthly atmospheric circulation data during 1961–2019 is derived from NCEP/NCAR Reanalysis (Kalnay et al., 1996). Herein, the mean June-July zonal and meridional atmospheric moisture fluxes (between 300 hPa and 1000 hPa) are calculated separately. Their magnitudes are then combined into the total integrated vapor transport (IVT, Wang & Yuan, 2018). The ensemble hindcast and forecast data from Climate Forecast System version 2 (CFSv2; Saha et al., 2014) that was operational at NCEP since March 2011, is also used in this study. In addition, the dispersion characteristics of the apparent Rossby wavetrain are also diagnosed using the wave activity flux (Takaya & Nakamura, 2001). Vertical integral of northward and eastward total energy flux from ECMWF Reanalysis v5 (ERA5; Hersbach et al., 2020) are also used to investigate the energy transportation from the TIO.

The IOBM index is defined as SST anomalies averaged over the tropical Indian Ocean (20°S-20°N, 40°-110°E), which is highly correlated with the first empirical orthogonal function (EOF) of SST variability over the same region (Yang et al., 2007) with a correlation coefficient of 0.98. The warm IOBM events are defined as the IOBM index greater than half of its standard deviation (0.5σ), and vice versa for the cold IOBM events. Moreover, the monthly Nino3.4 (Van Oldenborgh et al., 2021) and Pacific Decadal Oscillation (PDO; Mantua et al., 1997) indices used in this study are acquired from the KNMI Climate Explorer. Considering that the PDO is a robust interdecadal oscillation, a 21-year low-pass filtering based on the M-term Gaussian-Type Filter is performed to extract its interdecadal variability. A warm (cold) PDO phase corresponds to above (below) zero values. All anomalies are defined as deviations from the monthly climatology of 1981–2010. All the correlation coefficients analyses are conducted based on the detrended datasets to explore the year-to-year relationship between the IOBM and the dry-wet variation (including the corresponding circulation) over the WNWC.

2.2. Conditional Maximum Covariance Method

The relationship between TIO SST and WNWC precipitation is complex and always related to ENSO (Lu et al., 2019; Xie et al., 2002; Yang et al., 2007). Following An (2003), the conditional maximum covariance analysis (CMCA) is applied to detect the most coherent patterns between the precipitation over the WNWC and the tropical Indian SST fields, which not only can isolate the most coherent patterns between two fields but also exclude the unwanted signal. The method considers the precipitation and SST variables, $\xi^*(x, y, t)$ and $\psi^*(x, y, t)$ with a function of space (x, y) and time (t), and a time series Z(t) with a function of time only. Then, new variables $\xi(x, y, t)$ and $\psi(x, y, t)$ are defiend by removing the signal covariant with Z from ξ^* and ψ^*, respectively, as,

$$\xi = \xi^* - Z \times \frac{\text{cov}\,(\xi^*, Z)}{\text{var}(Z)} \quad \text{and}$$

$$\psi = \psi^* - Z \times \frac{\text{cov}\,(\psi^*, Z)}{\text{var}(Z)} \tag{1}$$

where cov and var indicate the temporal covariance between two variables and the variance, respectively. From the definition of Equation 1, cov(ξ, Z) and cov(ψ, Z) become zero at each spatial grid of ξ and ψ, which implies that the ξ and ψ are completely uncorrelated with Z. Using these newly defined variables ξ and ψ, the most coherent pairs of spatial patterns and their associated time series by performing an eigenanalysis on their temporal covariance matrix are isolated. Here, the NINO3.4 index is Z, which is removed to investigate the linkage of TIO SST and WNWC precipitation more clearly.

2.3. Statistical Forecasting Approach

Based on a linear regression in a cross-validation mode (Wang et al., 2017), a statistical forecasting approach utilizing the observed January-March mean IOBM index is developed to predict (hindcast) the April-June precipitation over the WNWC. For each April-June season in a 21-year sliding window, we establish a linear regression equation of PI using the IOBM in the preceding January-March in the remaining years: $PI_{(-s)} = a_s \times IOBM_{(-s)} + b_s$, where s is a given year, the variables with the subscripts $(-s)$ are information excluding the target year s, a_s and b_s are the corresponding regression coefficients. The statistical hindcasts of PI during April-June in a given year s is calculated in such a cross-validation mode. The skill of this forecast is evaluated by using the anomaly correlation (*AC*; Beckeret al., 2013; Wang & Yuan, 2018) between these two-time series, which is defined as $AC = \frac{\sum X'Y'}{[(X')^2(Y')^2]^{1/2}}$, where X′ is the observed precipitation anomaly and Y′ is the predicted counterparts in a given 21-year sliding window. According to a two-tailed Student's *t*-test, the 95% confidence level of *AC* is 0.42. By repeating this method with the 21-year window sliding, the *AC* value of each year can be obtained. In addition, the hit rate (*HR*) and false alarm rate (*FAR*) are also used to assess the forecast skill for severe hydrologic events (Ma et al., 2015; Wang & Yuan, 2018), where the severe wet (dry) condition is defined as the April-June mean precipitation greater (less) than 0.5σ (-0.5σ). Here, the HR and FAR are computed as

$$HR = \frac{m}{m+n}, FAR = \frac{p}{m+p} \tag{2}$$

where *m* is the number of events when a severe hydrologic event is both forecasted and observed, *n* is the number of events where an observed hydrologic event is not forecasted, and *p* is number of events where a hydrologic event is forecasted but not observed. Similar to the *AC* calculation, the time series of *HR* and *FAR* values can be obtained using the 21-year window sliding.

3. Results

3.1. Linkage Between the IOBM and WNWC Precipitation

Figure 2 shows the detrended annual precipitation and SST pattern in the first CMCA mode, with the explained variance of 80%. Basin-wide warming occurs over the TIO (Figure 2b), resembling the IOBM-like pattern described in previous studies (e.g., Xie et al., 2002). Temporal coefficients for the SST field are closely correlated with the IOBM index, with a correlation coefficient of 0.85 (*p-value* < 0.01, Figure 2c). When the IOBM is in its warm phase, most of the WNWC is in wetter conditions (Figure 2a). And the temporal coefficient of precipitation is in good agreement with that of the TIO SST, with a correlation coefficient of 0.59 (*p-value* < 0.01, Figure 2c). The detrended correlation between the annual precipitation and IOBM is calculated as 0.48 (*p-value* < 0.01).

To further examine the linkage between the IOBM and precipitation variability over the WNWC, the correlation coefficient distribution is plotted in Figure 3a. We can observe that the IOBM plays a crucial role in the annual precipitation across the entire WNWC region, particularly around the Tianshan Mountains, where precipitation mainly occurs and increased significantly (Shen et al., 2020; Shi et al., 2007). Previous studies indicated the significant seasonal variation of the IOBM, that is, it peaks in late boreal winter and early spring, and persists through boreal summer, following an El Niño event (Yang et al., 2007). Therefore, we also analyze the monthly
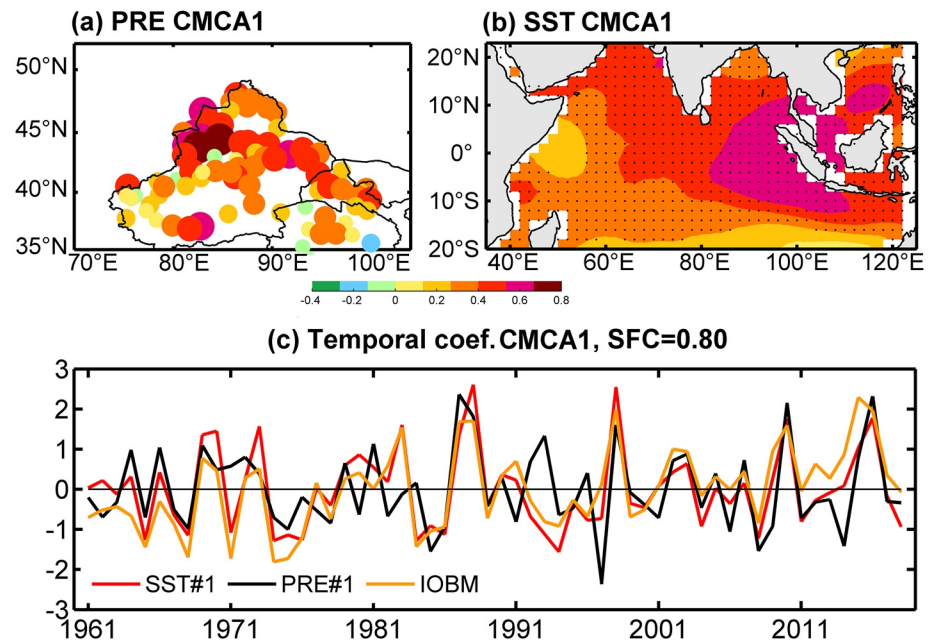
Figure 2. Temporal and spatial patterns of the CMCA1 modes for detrended precipitation over the western Northwest China (WNWC) and tropical Indian SST for 1961–2018. In the upper panels, (a) and (b) show the annual precipitation and SST anomaly represented by the CMCA1 mode, with red areas experiencing wetting (for precipitation) and warming (for SST). The variance explained by the CMCA1 is 80%. The corresponding temporal coefficient of the CMCA1 for precipitation (in black) and SST (in red), with the IOBM index (in orange) are shown in (c).

evolution of lag correlation coefficients (see Figure 3b). The basin TIO SST anomalies mainly influence the precipitation in April-June season, particularly in May. Since the IOBM SST leads the May precipitation by 0–5 months, the correlation coefficient values can reach 0.5. Notably, close correlations occur when the IOBM leads by 1–3 months. Such significant correlation does not appear when the IOBM SST lags the WNWC precipitation (figure is not shown). It implies that the TIO SST anomalies in preceding spring (January-March) are a significant predictor for the WNWC precipitation in April-June. It is worth noting that April-June season is the critical stage of crop emergence and growth in Xinjiang. Therefore, the precipitation deficiency or surplus during this period is prone to bring a series of adverse effect on the agricultural production and food quality, with the possibility of affecting the food security and social stability. In this sense, the close lagged correlation between the IOBM and precipitation provides some insight into precipitation prediction over the WNWC in late spring and early summer.

Nevertheless, the positive lagged relationship (above) is unstable and varies at the inter-decadal timescales. Figures 3c and 3d indicate the consistency of the variation of April-June or May precipitation over the WNWC with the preceding IOBM is much higher in the early decades and since the end of the twentieth century. While their year-to-year variability appears inconsistent during 1970s–1990s. For instance, during the most recent sub-period 1997–2018 (the dividing evidence is discussed in the next section), the correlation coefficient value between the IOBM index in the preceding January-March and WNWC precipitation in April-June was up to 0.71 (*p-value* < 0.01), far exceeding that during the former sub-period 1974–1996 (detrended correlation coefficient of 0.17; *p-value* = 0.44) and the whole studying period (detrended correlation coefficient of 0.45; *p-value* < 0.01). Take the different correlation distributions between January-March IOBM index and the subsequent April-June precipitation in WNWC in the 1974–1996 and 1997–2018 for example, the enhanced relationship can be seen clearly, as indicated in Figures 3e and 3f.

3.2. Interdecadal Influence of IOBM on WNWC Precipitation

To further investigate the varying relationship between IOBM and the precipitation variation over the WNWC, the 21-year running correlation coefficients between January-March IOBM and April-June precipitation over
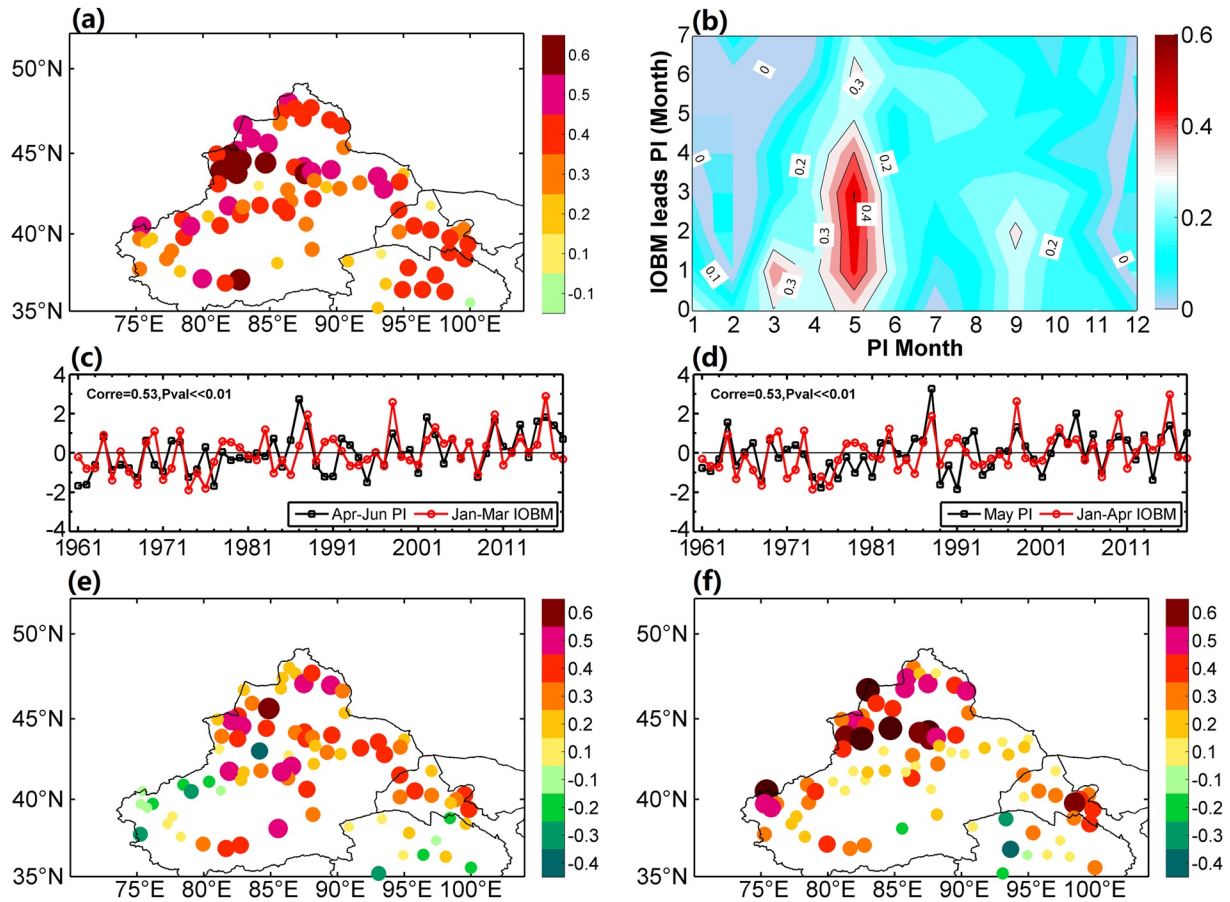
Figure 3. Correlation distribution and evolution of the IOBM index and precipitation over the WNWC for the period of 1961–2018. (a) Spatial distribution of the correlation coefficient between the annual IOBM index and precipitation over the WNWC. (b) Evolution of correlation coefficient between monthly precipitation over the WNWC and the IOBM at different lead time. In panel (b), x axis is the month of precipitation (PI) and y axis is the month of IOBM leading the precipitation; the red shaded areas have passed the significant level at 0.05. (c) Time series of the April-June PI over the WNWC and the IOBM index in the preceding January-March. (d) Same as (c), but for the time series of the May PI over the WNWC and the IOBM index in the preceding January-April. (e) Same as (a) but for January-March IOBM index and subsequent April-June precipitation over the WNWC for the sub-period of 1974–1996. (f) Same as (e) but for the sub-period of 1997–2018.

the WNWC are explored. Here the analysis is traced to an earlier period since 1951 to clarify the interdecadal influence of IOBM on WNWC precipitation, even though station-observed rainfall data before 1961 were fewer. As seen from Figure 4, the results show that this relationship is not robust during 1970s–90s, despite the positive correlation over the whole studying period. Before 1974 and from 1997 onward, these coefficients exceed 0.43, which is the threshold of 0.05 significance level. In the recent decades, high correlation (0.75) appears between the IOBM in January-March and WNWC precipitation in the following April-June (Figure 4a). The accumulative anomaly of the correlation coefficient also demonstrates that an interdecadal shift took place around 1974 and 1997 (Figure 4b). This result is consistent with several studies on the appearance of interdecadal transition of large-scale SST anomalies in the tropical Pacific in the middle of 1970s and late 1990s (Meehl & Arblaster, 2012; Wang et al., 2014). This indicates that the interdecadal lagged relationship of the WNWC precipitation and IOBM might be modulated by the PDO, related to the El Niño-like pattern of Pacific climate variability around 1976 and La Niña-like pattern in the late twentieth and early 21st centuries (Newman et al., 2016; Zhu et al., 2015).

To explore the possible mechanism of the interdecadal IOBM's impacting the WNWC precipitation, the seasonally evolving patterns of IOBM-related SST anomalies for the sub-periods of 1974–1996 and 1997–2018 are shown in Figure 5. Comparing with 1997–2016, the positive SST anomalies are relatively weaker in intensity and scope during 1974–1996. In addition, the strongest SST anomalies lies in the southern TIO near the equator during 1974–1996, while two additional warm centers are observed during 1997–2018, which are the Arabian Sea and the southwestern TIO. Particularly over the Arabian Sea, the averaged SST over 10°N-30°N, 50°E−74°E
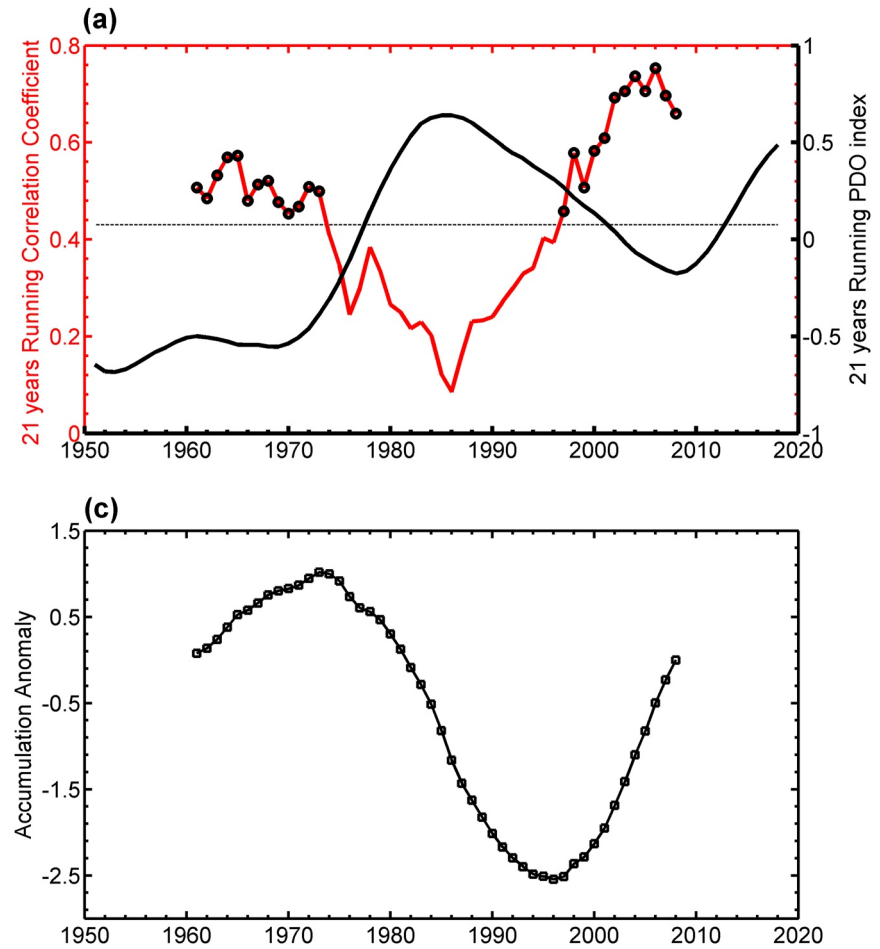
Figure 4. The evolution of (a) 21-year running correlation coefficient (in red) between January-March IOBM and April-June precipitation over the WNWC and (b) its accumulation anomaly. Straight line is the critical value (0.42) of the significant test at 0.05 level. The black curve in (a) is the decadal PDO index based on 21-year low-pass filter. The shift occurred in 1974 and 1997.

increases by 0.8 times and 1.5 times for January-February and April-June, respectively. Similary results are obtained after removing the ENSO. This decadal variability of TIO SST in intensity and location induce significant climate anomalies over the northern tropical zone, and exert a much significant impact on the Asian summer climate on the basis of the diagnostic analysis and numerical experiments (Qu & Huang, 2012; Sun et al., 2019). The correlation between the geopotential height fields and the IOBM in the previous January-March for the two sub-periods of 1974–1996 and 1997–2018 are further investigated (Figures 6 and 7). To remove the effect of the remote oceanic and atmospheric forcing of ENSO, a partial correlation analysis is performed via removing the signal of Niño 3.4 index during the two epochs. During the sub-period 1997–2018, the warm IOBM SST anomalies being a heating source near the equator can induce atmospheric responses of the like "Matsuno-Gill Pattern" (Hoerling et al., 2004; Yang et al., 2010, 2017). This atmospheric circulation anomaly appears to be an anomaly high center over the region around India Peninsula and Tibetan Plateau (Figure 6). A solid baroclinic structure appeared in the TIO region, with the negative anomaly at the bottom of the troposphere and the opposite anomaly at the upper troposphere (Figure 7). Comparing the IOBM-related simultaneous total energy flux in the two sub-periods, the energy is transported from the TIO to the India Peninsula and Eastern Europe when the IOBM is warm during 1997–2018 (Figure 8). The atmospheric circulation anomaly therefore appears to be an abnormally high pressure center over the region along the 30°N around the India Peninsula and Tibetan Plateau in subsequent April-June. Eastern Europe is dominated by significant high pressure anomalies as well (Figures 7d–7f). Then such anomalies further spread downstream to form a remote wave train along the jet axis in the mid-high latitude of the North hemisphere (Figures 6e–6h, Figure 8d). This wavetrain extends from Europe
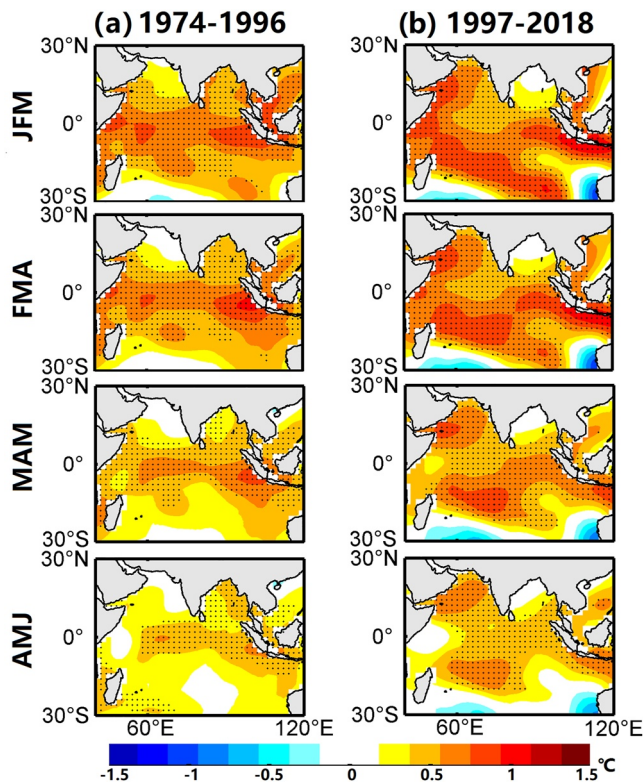
Figure 5. Seasonally evolving patterns of composited SST difference (unit: °C) between the warm and cold IOBM events for the sub-periods of 1974–1996 (a) and 1997–2018 (b), respectively. The dot sign denotes the IOBM-related SST anomalies are significant at a 0.05 level.

to the western North Pacific, with an anomalously negative pressure center around the Baikal Lake (termed as Baikal Low) and a significantly positive pressure center over the northwestern Pacific, as the IOBM is warmer in previous January-March (Figures 6 and 7). Most of the WNWC is dominated by the Baikal Low or located at its southern flanks (Figures 7d–7f). Under these circulations, the study region is dominated by enhanced westerly and southwesterly (Figures 9c and 9d), thereby transporting more water vapor to the WNWC region (as illustrated in Figure 10c). Meanwhile, the ascending motion also strengthens over most of the WNWC (Figure 10d), which is also partly advantageous to more precipitation in this region following a warming Indian Ocean with positive IOBM.

Moreover, TIO SST warming might be responsible for altering the climate in the North Atlantic by triggering a dipole pattern of circulation anomalies. A strengthening of both the Icelandic Low and Azores High can be observed during the sub-period of 1997–2018 (Figures 7d–7f). It implies that the warm IOBM can enhance the NAO pattern, verified by using the atmospheric general circulation model (AGCM) experiments (e.g., Bader & Latif, 2003; Hoerling et al., 2004; Mohtadi et al., 2014). The enhanced positive NAO contributes to the increased precipitation in WNWC (Hua et al., 2017).

During the warm PDO phase in 1974–1996, the TIO SST anomalies are obviously weaker than those during 1997–2018, and its center lies in south of Equator (Figure 5a). The regression distribution of circulation fields against IOBM shows obvious differences from those in the cold PDO phase of 1997–2018. The low-pressure anomalies over the Baikal Lake and WNWC are replaced by anomalously high pressure and corresponding downward movement (Figures 6a–6d, 7a–7c and 10b). North of it, the strange low pressure dominates the regions extending from Eastern Europe to Siberia. Influenced by this circulation pattern, the westerly is also enhanced over the WNWC. But it is much drier after the long transportation over Eurasia and the intensity is significantly smaller than that during 1997–2018 (Figure 10a).

Why are the above SST anomalies and the circulation response to IOBM in the cold PDO phase more significant than those in the warm PDO phase? The reason remains unclear. Generally, the PDO is positively correlated with the IOBM, via atmospheric and oceanic teleconnections (Cole et al., 2000; Huang et al., 2019). However, their relationship of decadal PDO and IOBM is not stationary and became negative in the past decades (Dong & McPhaden, 2017; Han et al., 2014; Hong et al., 2021). During the cold PDO phase of 1974–1996, the decadal relationship between the PDO and IOBM undergoes a shift from positive to negative. The SST anomalies of the TIO that were expected to be positive are counteracted by the opposite SST response to PDO and eventually dominated by weakly negative signal (Figures 11a and 11b). While the PDO enters a negative phase since the end of the twentieth century, the TIO stays warm and does not follow the PDO (Figures 11c and 11d). It to some extent contributes to the different SST anomalies in the warm phase of IOBM (Figure 5) and therefore a much significant impact on the middle latitudes in the cold PDO phase as mentioned above (Figures 6 and 7).

3.3. Interdecadal Variation in Rainfall Prediction

As mentioned earlier, the SST over the Pacific Ocean is associated with the influence of interdecadal fluctuations in IOBM on the climate of WNWC. Thus it might affect the prediction of precipitation. To determine it, a statistical forecasting (hindcast) approach based on the IOBM index in the preceding January-March season is used here to predict the April-June mean precipitation over the WNWC by using linear regression in a cross-validation mode (see Section 2). In Figure 12, the values of anomaly correlation (AC), hit rate (HR) and false alarm rate (FAR) are stratified according to the sign of the PDO index. During the cold phase of PDO, the AC value (0.43) is far above that in the warm PDO phase (AC value of only 0.03). It implies that the skill of April-June precipitation forecast over the WNWC based on the preceding IOBM signal in the cold PDO phase is much better than that during the warm PDO phase. Similar results are also obtained for both severely wet and dry events. There are
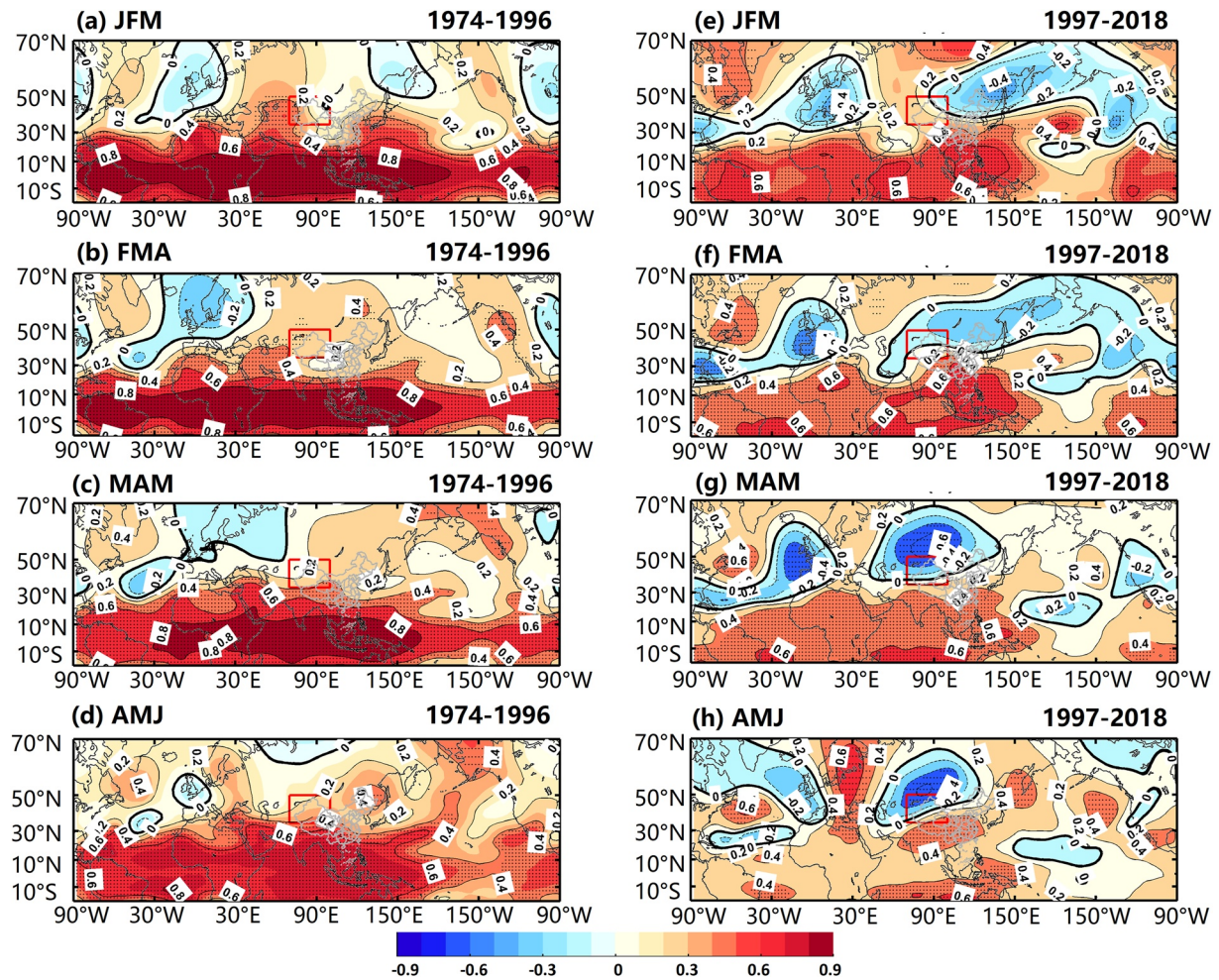
Figure 6. Seasonally evolving patterns of the partial correlation coefficient between 200 hPa geopotential height field and IOBM in January-March without ENSO signal for the sub-periods of 1974–1996 and 1997–2018, respectively. Red square box indicates the WNWC region. The dot sign indicates the correlation is significant at the 0.05 level.

fewer small *HR* values during the cold phase of PDO, but more large positive values (figure is not shown), with the mean value of 0.49 and 0.67 for severely wet and dry events respectively. These values are significantly higher (by performing a two sample *t*-test) than the *HR* values during the warm PDO phase, with the mean values of 0.33 and 0.32 for extremely wet and dry events, respectively.

Meanwhile, the FAR values are significantly low for the extremely dry and wet events during the cold PDO phase compared with those during the warm phase of PDO. Therefore, when the PDO is in the cold phase, the seasonal predictability of WNWC precipitation anomalies (based on a linear, lagged relationship with the IOBM) is significantly enhanced. Further comparison with the CFSv2 operational models verifies that the April-June precipitation forecast using the preceding January-March IOBM signal is more skillful than CFSv2 at the same lead time during the cold PDO phase, with the correlation coefficient increased by 7% (Figure 13). A study on the influence of ENSO on Australian climate also reported a similar outcome (Power et al., 1999). They indicated that the success of an ENSO-based statistical rainfall prediction in Australia varies with the Inter-decadal Pacific Oscillation and such interannual relationship is robust when the PDO is in its cold phase. Wang and Yuan (2008) also suggested that the influence of ENSO on the East Asian winter monsoon (EAWM) is insignificant in the warm phase of PDO, while ENSO can exert a strong impact on the EAWM, with cold temperature over East Asia during the cold phase of PDO.
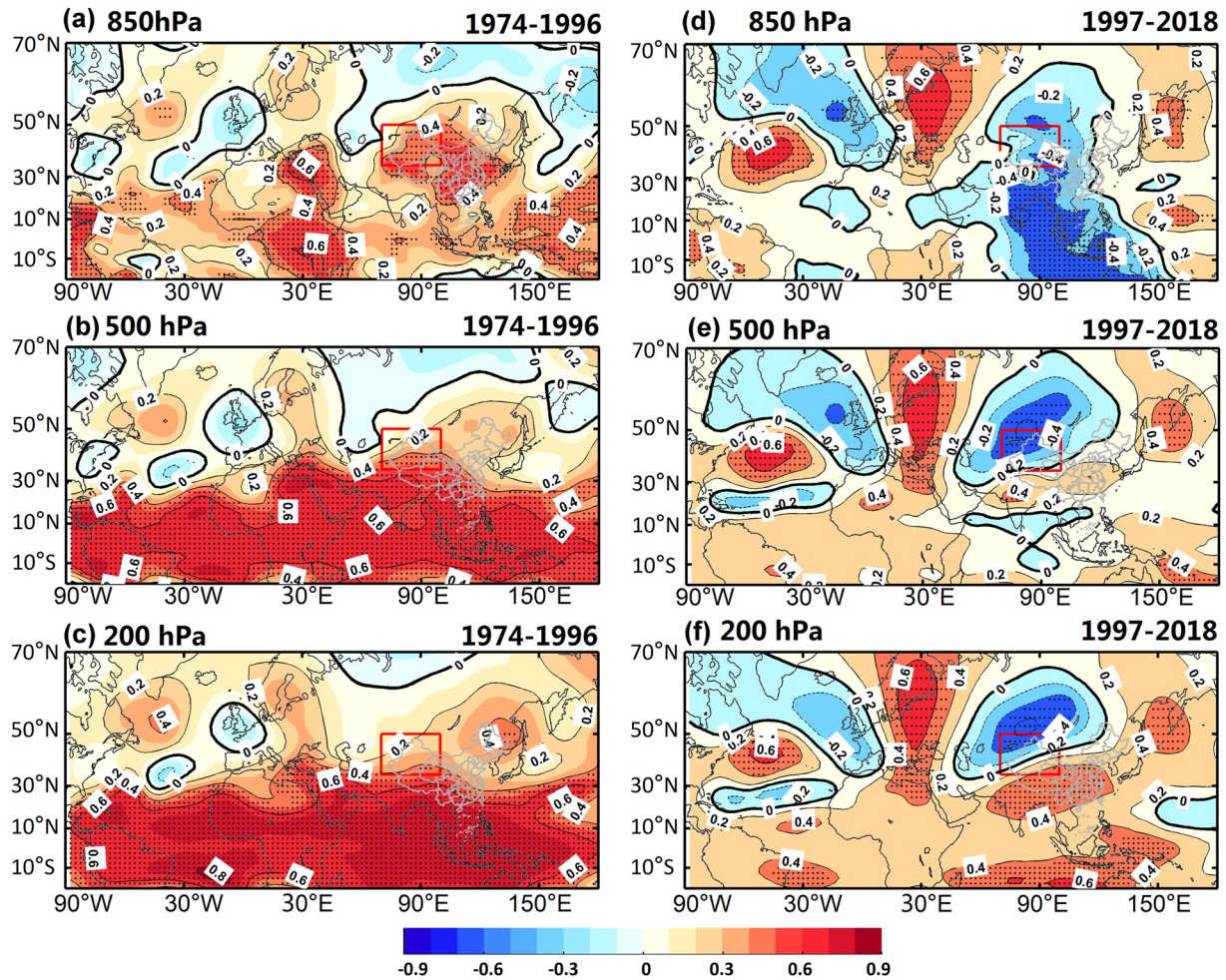
Figure 7. The partial correlation coefficient between the geopotential height field in April-June and IOBM in the previous January-March without ENSO signal for the sub-periods of 1974–1996 and 1997–2018, respectively. Red square box indicates the WNWC region. The dot sign indicates the correlation is significant at the 0.05 level.

4. Conclusions

As the dominant mode of Indian Ocean SST variability on interannual timescale, the IOBM always undergoes robust changes during ENSOs, acting like a capacitor lingering the effects of ENSO during summer after the dissipation of eastern Pacific SST anomalies (Xie et al., 2002). Nevertheless, not all IOBM events are induced by ENSO. Many studies have indicated that the IOBM is not just a passive response to ENSOs but also can independently force a Matsuno-Gill pattern in the upper troposphere with a strengthened South Asian High, thereby influencing the summer climate variability in East Asia and even in Northern Hemisphere (Schott et al., 2009; Yang et al., 2007). However, previous studies mostly concentrated on the influences of TIO SST on the climate over the African-Asian-Australian monsoon regions (Schott et al., 2009). For the arid and semi-arid regions in WNWC that are located in the innermost center of the Eurasia continent and far away from the surrounding oceans, the related research is much less, especially in a warmer current-climate, that many climatologist describes "a new normal" (Lewis et al., 2017), in which all weather events are different from those of the past.

Therefore, in this study, we extend previous studies on the relation between IOBM-linked climate variations and the WNWC region. Our results show that the year-to-year IOBM variability significantly impacts the year-to-year WNWC precipitation variability. However, such correlation varies significantly in different months or seasons. The significant lagged correlation just occurs between the IOBM SST variability in January-March and WNWC precipitation in the following April-June, especially in the following May. In other words, a positive IOBM with a basin-wide warming over TIO in January-March is usually followed by a wetter April-June over WNWC. It
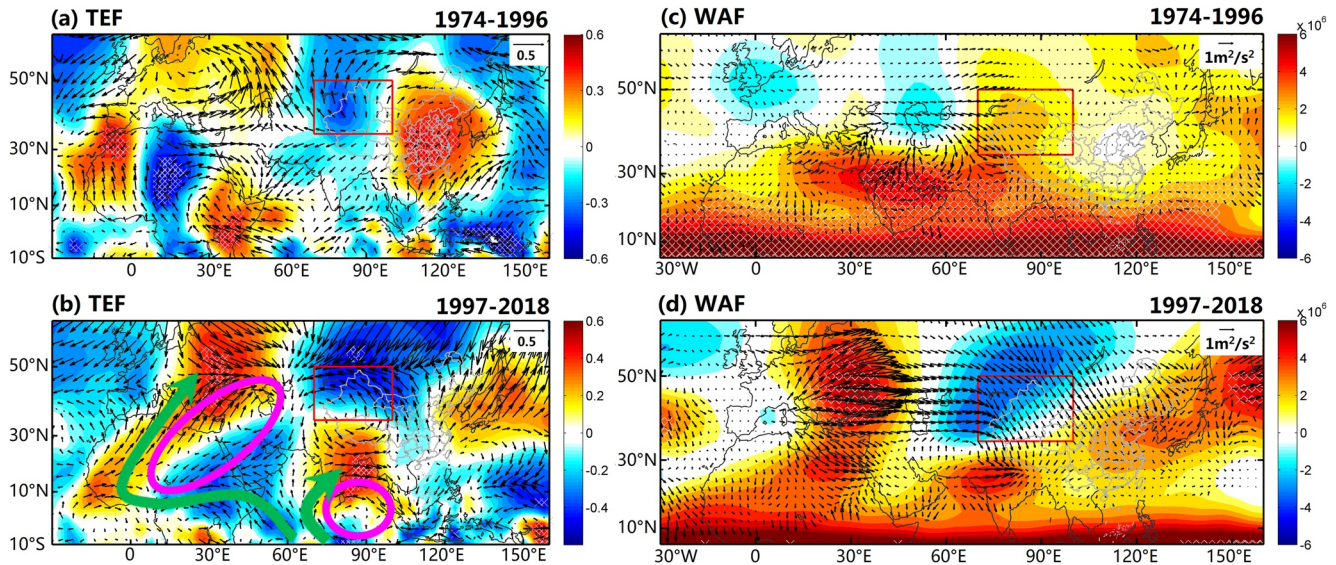
Figure 8. The simultaneous partial correlation coefficient between the vertical integral of total energy flux (TEF, vector) superimposed with the total energy (shading) and IOBM in the previous January-March without ENSO signal for the sub-periods of 1974–1996 (a) and 1997–2018 (b), respectively. The green arrow is the schematic diagram of energy transportation along the flank of anticyclone (purple ellipse). Red square box indicates the WNWC region. The dot sign indicates the correlation is significant at the 0.05 level. (c) The April-June mean QG stream function difference (shading, unit: m²/s) between the warm and cold IOBM events and their corresponding T-N wave activity flux (WAF, vector, unit: m²/s²) during 1974–1996. (d) is same as (c) for the sub-periods of 1997–2018.

implies that the IOBM in the preceding January-March could be a crucial predictor for the short-term prediction of April-June precipitation in the WNWC.

However, the lagged-relationship between the IOBM and WNWC precipitation is unstable and varies on the interdecadal timescale. The results suggested the association of this interdecadal fluctuation in the lagged-relationship between the IOBM and WNWC precipitation with the interdecadal SST variability in the Pacific Ocean, which is known as the Pacific Decadal Oscillation (PDO). In other words, the influence of the IOBM on WNWC
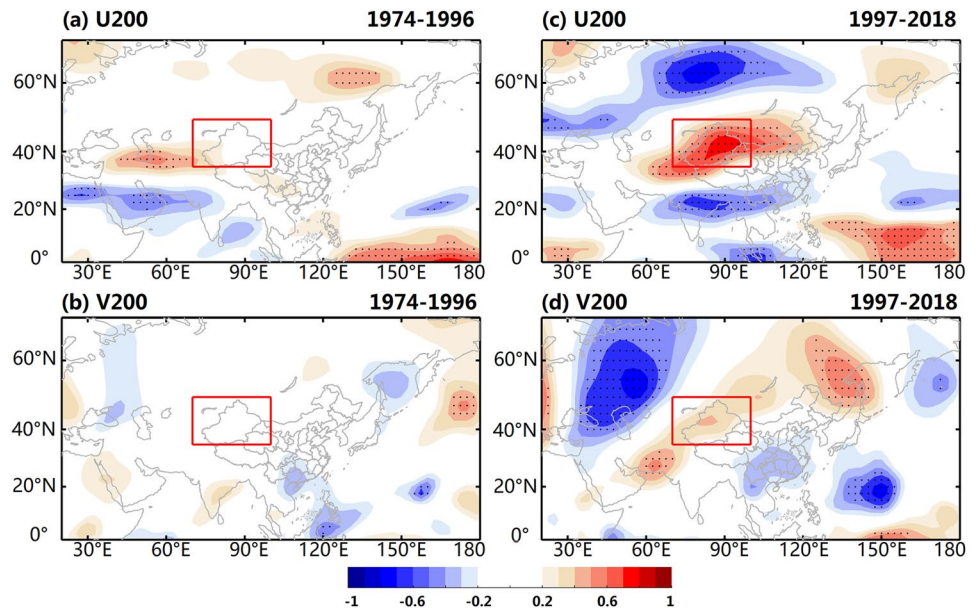

Figure 9. The partial correlation coefficient between zonal (in the upper panels) and IOBM in the previous January-March without ENSO signal for the sub-periods of 1974–1996 (a) and 1997–2018 (c). The bottom panels (b) and (d) are same as the (a) and (c) but for meridional wind at 200 hPa level. The dot signs indicate the correlation is significant at the 0.05 level.
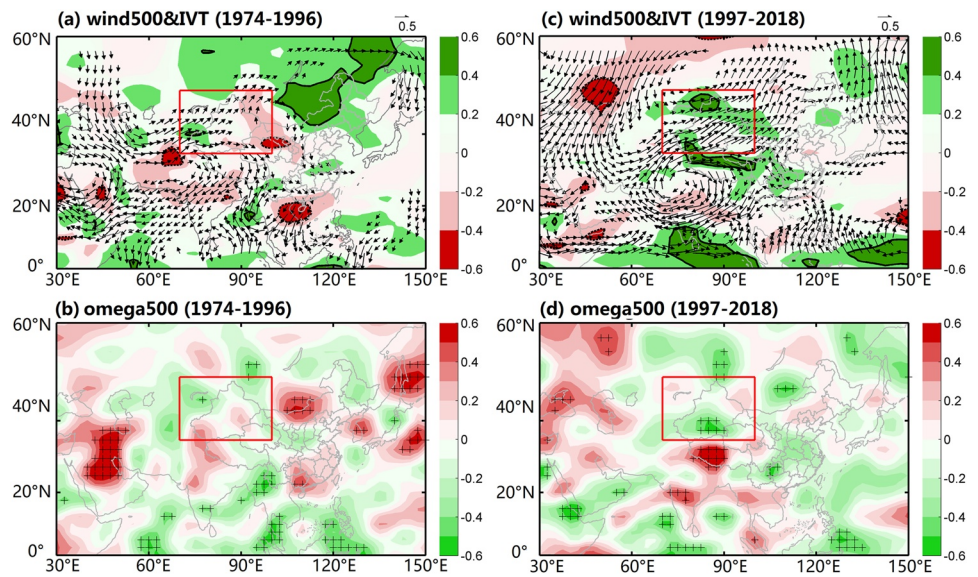
Figure 10. The partial correlation coefficient between horizontal wind (vector) field at 500 hPa superimposed with the integrated vapor transport (shading) and IOBM in the previous January-March without ENSO signal for the sub-periods of 1974–1996 (a) and 1997–2018 (c), respectively. The bottom panels (b) and (d) are same as the (a) and (c) but for the vertical velocity. The positive values of shading area in the bottom panels indicate vertical descending motion, while the negative values indicate vertical ascending motion. The black contours in the upper panels and the plus signs in the bottom panels indicate the correlation is significant at the 0.05 level.

precipitation is probably modulated by the interdecadal PDO signals. When the PDO is in its warm phase, there is no robust relationship between the WNWC precipitation variations and IOBM and the prediction scheme performs poorly.

While the PDO enters a negative phase since the end of the twentieth century, the TIO stays warm and does not follow the PDO. That is, the decadal IOBM was negatively correlated with the PDO during the cold PDO regime of 1997–2018, which is indicated to be attributed by the anthropogenic warming (Dong & McPhaden, 2017). This out-of phase relationship enhances the warm SST anomalies over the TIO, particularly over the Arabian Sea where the averaged SST increases by 1.5 times for April-June. Similar results are obtained after removing the ENSO. Under the combined influence mentioned above, the IOBM-related SST anomalies are robust during the
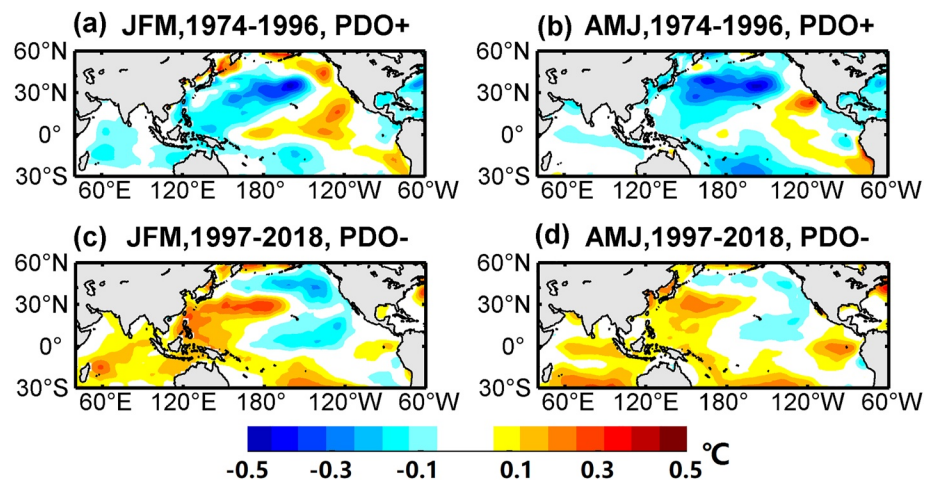

Figure 11. Indo-Pacific basin SST anomalies (°C) averaged for January-March (a) and April-June (b) during the cold PDO periods of 1974–1996, with the linear trend removed. The bottom panels (c) and (d) are same as the upper panels but for the cold PDO phase of 1997–2018, respectively.
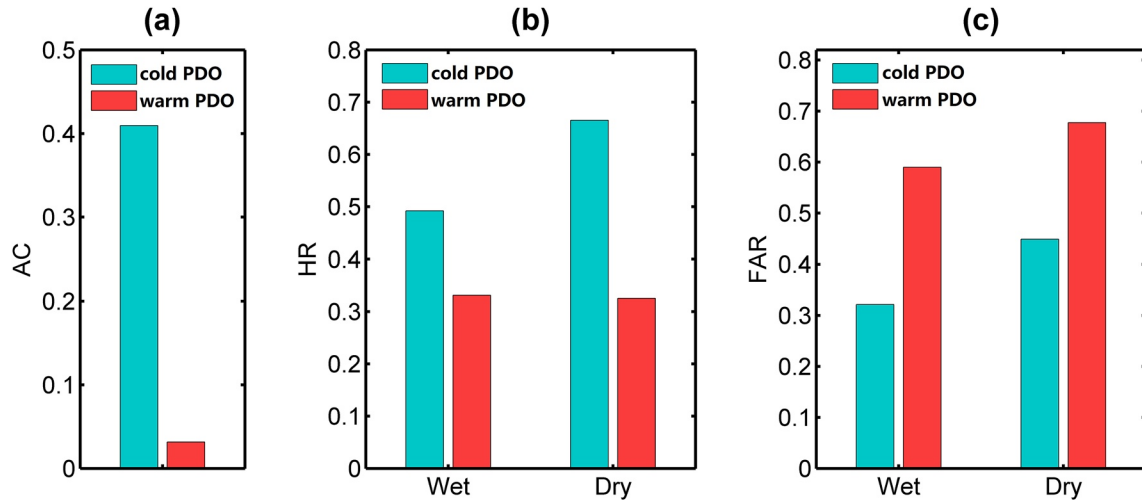
Figure 12. The forecast skill at different PDO phases. (a) Anomaly correlation (*AC*) for precipitation, (b) the hit rate (*HR*) and (c) false alarm rate (*FAR*) for extremely wet (≥0.5σ) and dry events (≤−0.5σ) across the WNWC region conditioned on the cold (in turquoise) and warm (in red) phases of PDO. Here, cPDO and wPDO denote the cold and warm PDO phase, respectively.

cold PDO phase of 1997–2018. This significantly warm IOBM SST anomalies being a heating source near the equator can induce a Matsuno–Gill response in the upper troposphere. The atmospheric circulation anomaly appears to be a high anomaly center over the region around India Peninsula and Tibetan Plateau. Further, it spreads downstream to form a remote wave train along the jet axis in the mid-high latitude of the Northern Hemisphere. The WNWC is dominated by the strange circulation pattern of "north low (Baikal Low) and south high (South Asia High)," thereby enhancing the southwesterly which transports additional moisture from the Arabian Sea and TIO to the study region. Accompanied by the enhanced upward motion, they are jointly advantageous to more precipitation in WNWC and contribute to the wetting climate over the WNWC in recent decades. What is more, the association between IOBM and WNWC precipitation is strong and the predictive scheme performs well in the cold phase of PDO. This result is similar to that of Power et al. (1999) who indicated that the robust relationship between year-to-year Australian climate variations and ENSO only occurs during the cold phase of PDO.

Moreover, the WNWC region has experienced detectable warming and wetting trends in recent decades. The increase in precipitation during April-June contributes about 35% of wetting in this region. After the 1960s, both the mean SST and the TIO SST variability amplitude gradually increased (Qu & Huang, 2012). Aided by the enhancing influence of the IOBM on WNWC precipitation, they jointly contribute to the wetting climate over the WNWC in recent decades. Furthermore, April-June is the key stage of heading and growing for crops, and the precipitation deficit during this period is known as the "strangle hold" drought (Yang et al., 2015). Therefore predicting the precipitation variation in advance is essential for local water resource management and hazard mitigation. In the end of the twentieth century, the PDO has entered a cold phase with colder SSTs in the eastern tropical Pacific Ocean. The lagged relationship between the IOBM and WNWC precipitation gets much closer, which enhances the forecast skill. Moreover, the IOBM is predictable beyond the 6-month lead and can be adequately simulated using coupled general circulation models (Saji et al., 2006). Consequently, the change and variability of IOBM should be considered as a significant predictor in improving seasonal prediction for the dry-wet events over the arid and semi-arid regions of WNWC shortly when the PDO is in its cold phase.
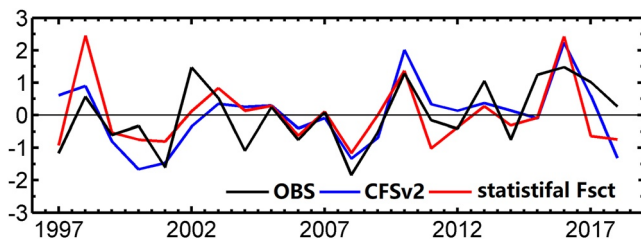

Figure 13. Standardized time series of observed and predicted precipitation over WNWC for the period of 1997–2018. The black curve is the observed precipitation, the red curve is the statistical forecast which is based on the linearly regressing precipitation against the January-March IOBM index, and the blue curve is the CFSv2 predicted precipitation at the same lead time, which is averaged from 72 ensemble members through January-March (start from January).

Data Availability Statement

The observed precipitation data are provided by the National Meteorological Information Center (NMIC) in China Meteorological Administration (http://data.cma.cn/). The monthly sea surface temperature (SST) is available from

NOAA Extended Reconstructed SST, version 5 (ERSST.v5, https://psl.noaa.gov/data/gridded/data.noaa.ersst.v5.html). The circulation variables including the geopotential height, u- and v-wind, vertical velocity, specific humidity are available from the NCEP/NCAR Reanalysis project (https://psl.noaa.gov/data/gridded/data.ncep.reanalysis.html). The vertical integral of total energy are provided by ECMWF's ERA5 reanalysis (https://cds.climate.copernicus.eu/cdsapp#!/dataset/reanalysis-era5-single-levels-monthly-means?tab=overview), and the Nino3.4 and PDO indice are provided by the KNMI Climate Explorer (http://climexp.knmi.nl/selectindex.cgi?id=someone@somewhere). In addition, the NCEP's CFSv2 hindcast and forecast data are available from (http://iridl.ldeo.columbia.edu/SOURCES/.Models/.NMME/.NCEP-CFSv2/). All data used in this paper are available at the time of submission. *Figures in this manuscript were made with MATLAB version 2020a and this software is available from* http://www.mathworks.com/ (The Math Works, Inc., 2020).

References

An, S.-II. (2003). Conditional maximum covariance analysis and its application to the tropical Indian ocean SST and surface wind stress anomalies. *Journal of Climate*, *16*(17), 2932–2938. https://doi.org/10.1175/1520-0442(2003)016%3C2932:CMCAAI%3E2.0.CO;2

Bader, J., & Latif, M. (2003). The impact of decadal-scale Indian Ocean sea surface temperature anomalies on Sahelian rainfall and the North Atlantic Oscillation. *Geophysical Research Letters*, *30*(22), 2169. https://doi.org/10.1029/2003gl018426

Becker, E. J., van den Dool, H., & Peña, M. (2013). Short-term climate extremes: Prediction skill and predictability. *Journal of Climate*, *26*(2), 512–531. https://doi.org/10.1175/jcli-d-12-00177.1

Chen, C., Zhang, X., Lu, H., Jin, L., Du, Y., & Chen, F. (2021). Increasing summer precipitation in arid central Asia linked to the weakening of the EastAsian summer monsoon in the recent decades. *International Journal of Climatology*, *41*(2), 1024–1038. https://doi.org/10.1002/joc.6727

Chen, F., Chen, J., & Huang, W. (2021). Weakened East Asian summer monsoon triggers increased precipitation in Northwest China. *Science China Earth Sciences*, *64*(5), 835–837. https://doi.org/10.1007/s11430-020-9731-7

Chen, G., & Huang, R. (2012). Excitation mechanisms of the teleconnection patterns affecting the July precipitation innorthwest China. *Journal of Climate*, *25*(22), 7834–7851. https://doi.org/10.1175/JCLI-D-11-00684.1S

Chen, Y., Li, Z., Fan, Y., Wang, H., & Deng, H. (2015). Progress and prospects of climate change impacts on hydrology in the arid region of northwest China. *Environmental Research*, *139*, 11–19. https://doi.org/10.1016/j.envres.2014.12.029

Cole, J. E., Dunbar, R. B., McClanahan, T. R., & Muthiga, N. A. (2000). Tropical Pacific forcing of decadal SST variability in the Western Indian Ocean over the past two centuries. *Science*, *287*(5453), 617–619. https://doi.org/10.1126/science.287.5453.617

Dai, X. G., Li, W. J., Ma, Z. G., & Wang, P. (2007). Water-vapor source shift of Xinjiang region during the recent twenty years. *Progress in Natural Science*, *17*(5), 569–575. https://doi.org/10.1080/10020070708541037

Dong, L., & McPhaden, M. J. (2017). Why has the relationship between Indian and Pacific Ocean decadal variability changed in recent decades? *Journal of Climate*, *30*(6), 1971–1983. https://doi.org/10.1175/JCLI-D-16-0313.1

Drumond, A., Nieto, R., & Gimeno, L. (2011). Sources of moisture for China and their variations during drier and wetter conditions in 2000–2004: A Lagrangian approach. *Climate Research*, *50*(2), 215–225. https://doi.org/10.3354/cr01043

Han, W., Meehl, G. A., Hu, A., Alexander, M. A., Yamagata, T., Yuan, D., et al. (2014). Intensification of decadal and multidecadal sea level variability in the Western tropical Pacific during recent decades. *Climate Dynamics*, *43*(5–6), 1357–1379. https://doi.org/10.1007/s00382-013-1951-1

Hersbach, H., Bell, B., Berrisford, P., Hirahara, S., Horányi, A., Muñoz-Sabater, J., et al. (2020). The ERA5 global reanalysis [Dataset]. Quarterly Journal of the Royal Meteorological Society, *146*(730), 1999–2049. https://doi.org/10.1002/qj.3803

Hoerling, M. P., Hurrell, J. W., Xu, T., Bates, G. T., & Phillips, A. S. (2004). Twentieth century North Atlantic climate change. Part II: Understanding the effect of Indian Ocean warming. *Climate Dynamics*, *23*(3–4), 391–405. https://doi.org/10.1007/s00382-004-0433-x

Hong, J.-S., Yeh, S.-W., Yang, Y.-M., Lim, Y.-K., & Kim, K.-M. (2021). *Understanding the weakening relationship of the pacific decadal oscillation and Indian Ocean basin mode during boreal winter*. Climate Dynamics. https://doi.org/10.21203/rs.3.rs-640927/v1

Hua, L., Zhong, L., & Ma, Z. (2017). Decadal transition of moisture sources and transport in northwestern China during summer from 1982 to 2010. *Journal of Geophysical Research: Atmospheres*, *122*(23), 12522–12540. https://doi.org/10.1002/2017JD027728

Huang, B. Y., Thorn, P. W., Banzon, V. F., Boyer, T., Chepurin, G., Lawrimore, J. H., et al. (2017). Extended Reconstructed Sea surface temperature version 5 (ERSSTv5), upgrades, validations, and intercomparisons [Dataset]. Journal of Climate, *30* (20), 8179–8205. https://doi.org/10.1175/JCLI-D-16-0836.1

Huang, J., Li, Y., Dai, A., Chen, F., Fu, Q., & Wang, G. (2017). Dryland climate change: Recent progress and challenges. *Review of Geophysics*, *55*(3), 719–778. https://doi.org/10.1002/2016RG000550

Huang, J., Zhang, W., Zuo, J., Bi, J., Shi, J., Wang, X., et al. (2008). An overview of the semi-arid climate and environment research observatory over the Loess Plateau. *Advances in Atmospheric Sciences*, *25*(6), 1–16. https://doi.org/10.1007/s00376-008-0906-7

Huang, W., Feng, S., Chen, J., & Chen, F. (2015). Physical mechanisms of summer precipitation variations in the Tarim Basin in northwestern China. *Journal of Climate*, *28*(9), 3579–3591. https://doi.org/10.1175/JCLI-D-14-00395.1

Huang, Y., Wu, B., Li, T., Zhou, T., & Liu, B. (2019). Interdecadal Indian Ocean basin mode driven by interdecadal Pacific oscillation: A season-dependent growth mechanism. *Journal of Climate*, *32*(7), 2057–2073. https://doi.org/10.1175/JCLI-D-18-0452.1

Kalnay, E., Kanamitsu, M., Kistler, R., Collins, W., Deaven, D., Gandin, L., et al. (1996). The NCEP/NCAR 40-year reanalysis project [Dataset]. Bulletin America Meteorology Social, *77*, 437–470. https://doi.org/10.1175/1520-0477(1996)077%3C0437:TNYRP%3E2.0.CO;2

Koster, R. D., Dirmeyer, P. A., Guo, Z., Bonan, G., Chan, E., Cox, P., et al. (2004). Regions of strong coupling between soil moisture and precipitation. *Science*, *305*(5687), 1138–1140. https://doi.org/10.1126/science.1100217

Kucharski, F., Molteni, F., & Yoo, J. H. (2006). SST forcing of decadal Indian Monsoon rainfall variability. *Geophysical Research Letters*, *33*(3), L03709. https://doi.org/10.1029/2005GL025371

Lewis, S. C., King, A. D., & Perkins-Kirkpatrick, S. E. (2017). Defining a new normal for extremes in a warming world. *Bulletin America Meteorology Social*, *98*(6), 1139–1151. https://doi.org/10.1175/BAMS-D-16-0183.1

Li, L., Yang, S., Zhu, X., Wang, Z., & Tang, H. (2010). Evidence of warming and wetting climate over the Qinghai-Tibet Plateau. *Arctic Antarctic and Alpine Research*, *42*(4), 449–457. https://doi.org/10.1657/1938-4246-42.4.449

Li, M., & Ma, M. (2018). Decadal changes in summer precipitation over arid northwest China and associated atmospheric circulations. *International Journal of Climatology*, *38*(12), 4496–4508. https://doi.org/10.1002/joc.5682

Li, Q., Yang, S., Kousky, V. E., Higgins, R. W., Lau, K.-M., & Xie, P. (2005). Features of cross-Pacific climate shown in the variability of China and US precipitation. *International Journal of Climatology*, *25*(13), 1675–1696. https://doi.org/10.1002/joc.1271

Lu, B., Li, H. Y., Wu, J., Zhang, T., Liu, J., Liu, B., et al. (2019). Impact of El Nino and southern oscillation on the summer precipitation over Northwest China. *Atmospheric Science Letters*, *20*(8), e928. https://doi.org/10.1002/asl.928

Ma, F., Yuan, X., & Ye, A. (2015). Seasonal drought predictability and forecast skill over China. *Journal of Geophysical Research: Atmospheres*, *120*(16), 8264–8275. https://doi.org/10.1002/2015JD023185

Mantua, N. J., Hare, S. R., Zhang, Y., Wallace, J. M., & Francis, R. C. (1997). A Pacific interdecadal climate oscillation with impacts on salmon production. *Bulletin of the American Meteorological Society*, *78*(6), 1069–1079. https://doi.org/10.1175/1520-0477(1997)078<1069:APICOW>2.0.CO;2

Meehl, G. A., & Arblaster, J. M. (2012). Relating the strength of the tropospheric biennial oscillation (TBO) to the phase of the Interdecadal Pacific Oscillation (IPO). *Geophysical Research Letters*, *39*(20), L20716. https://doi.org/10.1029/2012GL053386

Mohtadi, M., Prange, M., Oppo, D., Pol-Holz, R., Merkel, U., Zhang, X., et al. (2014). North Atlantic forcing of tropical Indian Ocean climate. *Nature*, *509*(7498), 76–80. https://doi.org/10.1038/nature13196

Newman, M., Alexander, M. A., Ault, T. R., Cobb, K. M., Deser, C., Di Lorenzo, E., et al. (2016). The Pacific decadal oscillation, revisited. *Journal of Climate*, *29*(12), 4399–4427. https://doi.org/10.1175/JCLI-D-15-0508.1

Peng, D., & Zhou, T. (2017). Why was the arid and semiarid northwest China getting wetter in the recent decades? *Journal of Geophysical Research: Atmospheres*, *122*(17), 9060–9075. https://doi.org/10.1002/2016JD026424

Power, S., Casey, T., Folland, C., Colman, A., & Mehta, V. (1999). Inter-decadal modulation of the impact of ENSO on Australia. *Climate Dynamics*, *15*(5), 319–324. https://doi.org/10.1007/s003820050284

Qu, X., & Huang, G. (2012). An enhanced influence of tropical Indian ocean on the south Asia high after the late 1970s. *Journal of Climate*, *25*(20), 6930–6941. https://doi.org/10.1175/JCLI-D-11-00696.1

Ren, Z. H., Yu, Y., Zou, F. L., & Xu, Y., (2012). Quality detection of surface historical basic meteorological data [Dataset]. Journal of Applied Meteorological Science, (In Chinese), *23*, 739–747. Retrieved from http://qikan.camscma.cn/jamsweb/article/id/20120611

Saha, S., Moorthi, S., Wu, X., Wang, J., Nadiga, S., Tripp, P., et al. (2014). The NCEP climate forecast system version 2 [Dataset]. Journal of Climate, *27*, 2185–2208. https://doi.org/10.1175/JCLID-12-00823.1

Saji, N. H., Xie, S.-P., & Yamagata, T. (2006). Tropical Indian Ocean variability in the IPCC 20th-century climate simulations. *Journal of Climate*, *19*(17), 4397–4417. https://doi.org/10.1175/JCLI3847.1

Schott, F. A., Xie, S.-P., & McCreary, J. P. (2009). Indian Ocean circulation and climate variability. *Review of Geophysics*, *47*(1), RG1002. https://doi.org/10.1029/2007rg000245

Shen, Y.-J., Shen, Y., Gao, Y., Zhang, Y., Pei, H., & Brenning, A. (2020). Review of historical and projected future climatic and hydrological changes in mountainous semiarid Xinjiang (northwestern China), central Asia. *Catena*, *187*, 104343. https://doi.org/10.1016/j.catena.2019.104343

Shi, Y., Shen, Y., Kang, E., Li, D., Ding, Y., Zhang, G., & Hu, R. (2007). Recent and future climate change in northwest China. *Climate Change*, *80*(3–4), 379–393. https://doi.org/10.1007/s10584-006-9121-7

Sun, B., Li, H. X., & Zhou, B. T. (2019). Interdecadal variation of Indian Ocean basin mode and the impact on Asian summer climate. *Geophysical Research Letters*, *46*(21), 12388–12397. https://doi.org/10.1029/2019gl085019

Takaya, K., & Nakamura, H. (2001). A formulation of a phase-independent wave-activity flux for stationary and migratory quasi-geostrophic eddies on a zonally varying basic flow. *Journal of the Atmospheric Sciences*, *58*(6), 608–627. https://doi.org/10.1175/1520-0469(2001)058<0608:afoapi>2.0.co;2

The Math Works, Inc. (2020). MATLAB (Version 2020a). [software]. Zenodo. Retrieved from http://www.mathworks.com/

Van Oldenborgh, G. J., Hendon, H., Stockdale, T., L'Heureux, M., De Perez, E. C., Singh, R., & Van Aalst, M. (2021). Defining El Niño indices in a warming climate. *Environmental Research Letters*, *16*(4), 044003. https://doi.org/10.1088/1748-9326/abe9ed

Wang, H., Chen, Y., & Pan, Y. (2015). Characteristics of drought in the arid region of northwestern China. *Climate Research*, *62*(2), 99–113. https://doi.org/10.3354/cr01266

Wang, S., Huang, J., He, Y., & Guan, Y. (2014). Combined effects of the Pacific decadal oscillation and El Nino-southern oscillation on global land dry–wet changes. *Scientific Reports*, *4*(1), 6651. https://doi.org/10.1038/srep06651

Wang, S., & Yuan, X. (2018). Extending seasonal predictability of Yangtze River summer floods. *Hydrology and Earth System Sciences*, *22*(8), 4201–4211. https://doi.org/10.5194/hess-22-4201-2018

Wang, S., Yuan, X., & Li, Y. (2017). Does a strong El Niño imply a higher predictability of extreme drought? *Scientific Reports*, *7*(1), 40741. https://doi.org/10.1038/srep40741

Wang, S. P., Zhang, Q., Yue, P., & Wang, J. (2020). Effects of evapotranspiration and precipitation on dryness/wetness changes in China. *Theoretical and Applied Climatology*, *142*(3–4), 1027–1038. https://doi.org/10.1007/s00704-020-03336-8

Xie, S.-P., Annamalai, H., Schott, F. A., & McCreary, J. P. (2002). Structure and mechanisms of south Indian Ocean climate variability. *Journal of Climate*, *15*(8), 864–878. https://doi.org/10.1175/1520-0442(2002)015<0864:SAMOSI>2.0.CO;2

Yang, J. L., Hu, H. B., Mu, J. H., Wang, M., & Hu, W. D. (2017). Study of numerical model stimulation of the tropical Indian Ocean basin mode impacts on May precipitation anomaly in east of Northwest China. *Plateau Meteorology*, *36*, 510–516. https://doi.org/10.7522/j.issn.1000-0534

Yang, J. L., Li, Y. C., Mu, J. H., & Wang, S. Y. (2015). Analysis of relationship between sea surface temperature in tropical Indian ocean and precipitation in East of Northwest China. *Plateau Meteorology*, *34*(3), 690–699. https://doi.org/10.7522/j.issn.1000-0534.2014.00010

Yang, J. L., Liu, Q. Y., & Liu, Z. Y. (2010). Linking observations of the Asian monsoon to the Indian Ocean SST: Possible roles of Indian Ocean basin mode and dipole mode. *Journal of Climate*, *23*(21), 5889–5902. https://doi.org/10.1175/2010JCLI2962.1

Yang, J. L., Liu, Q. Y., Xie, S. P., Liu, Z. Y., & Wu, L. X. (2007). Impact of the Indian Ocean SST basin mode on the Asian summer monsoon. *Geophysical Research Letters*, *34*(2), L02708. https://doi.org/10.1029/GL028571

Yao, J. Q., Chen, Y. N., Zhao, Y., Guan, X. F., Miao, W. Y., & Yang, L. M. (2020). Climatic and associated atmospheric water cycle changes over the Xinjiang, China. *Journal of Hydrology*, *585*, 124823. https://doi.org/10.1016/j.jhydrol.2020.124823

Zhang, J., Chen, H., & Zhang, Q. (2019). Extreme drought in the recent two decades in northern China resulting from Eurasian warming. *Climate Dynamics*, *52*(5–6), 2885–2902. https://doi.org/10.1007/s00382-018-4312-2

Zhang, Q., Lin, J., Liu, W., & Han, L. (2019). Precipitation seesaw phenomenon and its formation mechanism in the eastern and Western parts of Northwest China during the flood season. *Science China Earth Sciences*, *62*(12), 2083–2098. https://doi.org/10.1007/s11430-018-9357-y

Zhang, Q., Yang, Z., Hao, X., & Yue, P. (2019). Conversion features of evapotranspiration responding to climate warming in transitional climate regions in northern China. *Climate Dynamics*, *52*(7–8), 3891–3903. https://doi.org/10.1007/s00382-018-4364-3

Zhu, Y., Wang, H., Ma, J., Wang, T., & Sun, J. (2015). Contribution of the phase transition of Pacific Decadal Oscillation to the late 1990s' shift in East China summer rainfall. *Journal of Geophysical Research: Atmospheres*, *120*(17), 8817–8827. https://doi.org/10.1002/2015JD023545